Supporting Information for:

A universal deposition protocol for planar heterojunction solar cells with high efficiency based on hybrid lead halide perovskite families

Bert Conings,*[a,b] Aslihan Babayigit,[a,b] Matthew T. Klug,[b] Sai Bai,[b, c] Nicolas Gauquelin,[d] Nobuya Sakai,[b] Jacob Tse-Wei Wang,[b] Johan Verbeeck,[d] Hans-Gerd Boyen,[a] Henry J. Snaith*[b]

[a] Hasselt University, Institute for Materials Research, Wetenschapspark 1, 3590 Diepenbeek, Belgium. E-mail: bert.conings@uhasselt.be

[b] Clarendon Laboratory, Department of Physics, University of Oxford, Oxford OX1 3PU, United Kingdom. Email: henry.snaith@physics.ox.ac.uk

[c] Biomolecular and Organic Electronics, IFM, Linköping University, Linköping 58183, Sweden.

[d] Electron Microscopy for Materials Research (EMAT), University of Antwerp, Groenenborgerlaan 171, 2020 Antwerp, Belgium.

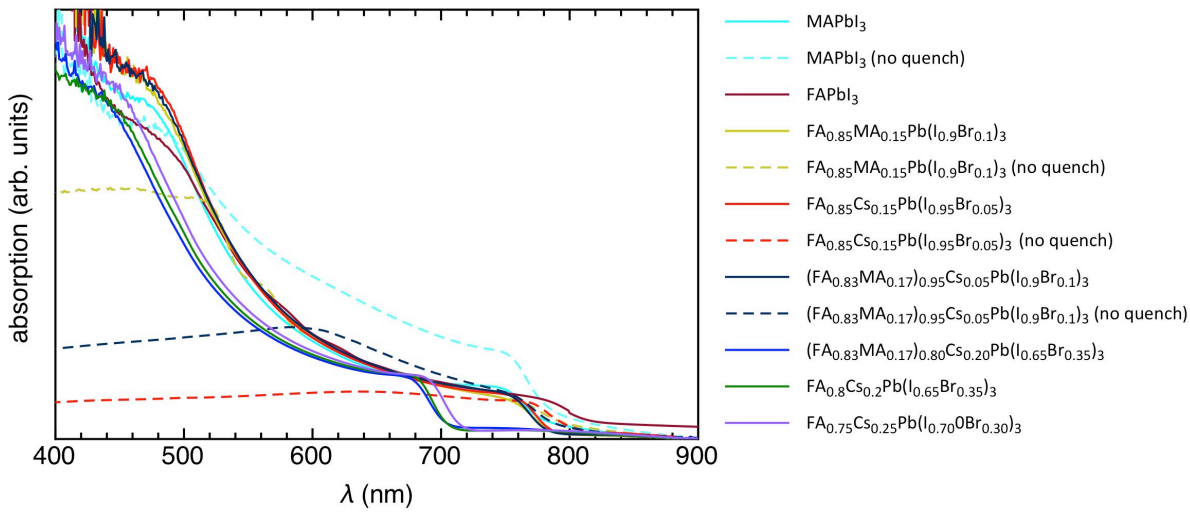

Fig. S1: Optical absorption spectra of the perovskite films in this work. The films were deposited on glass.

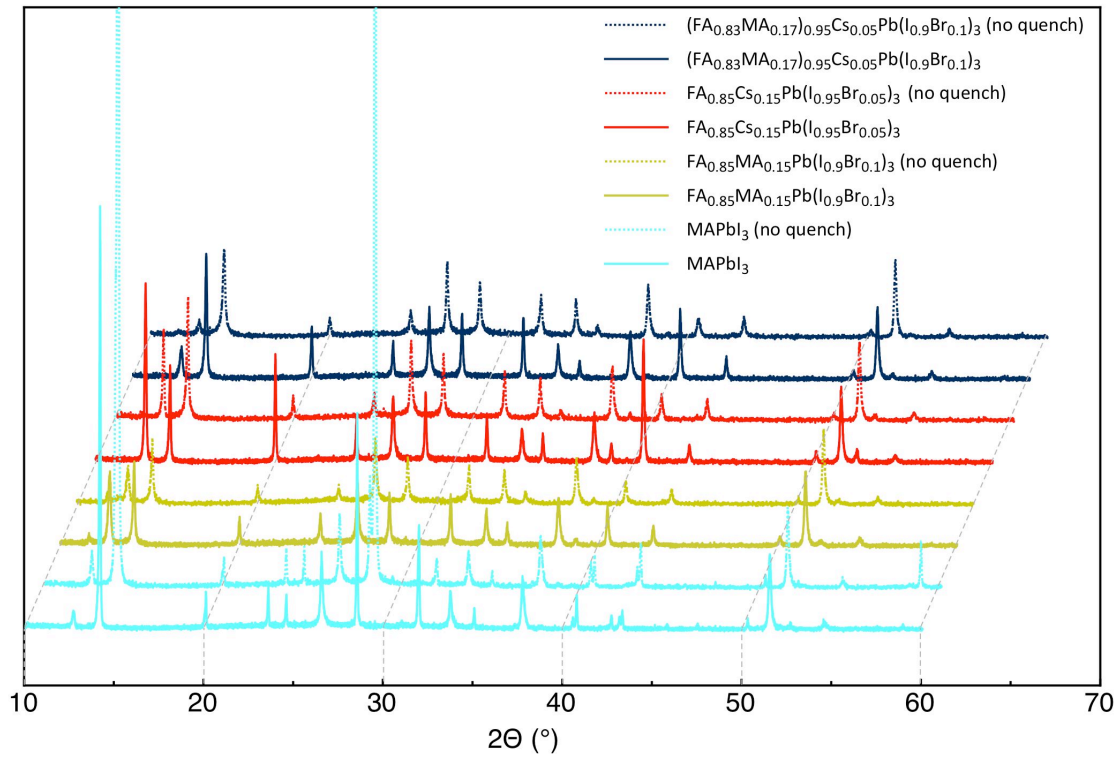

Fig. S2: X-ray diffraction data comparing gas quenched and non-quenched versions for a subset of the perovskites in this work. The films were deposited on FTO.

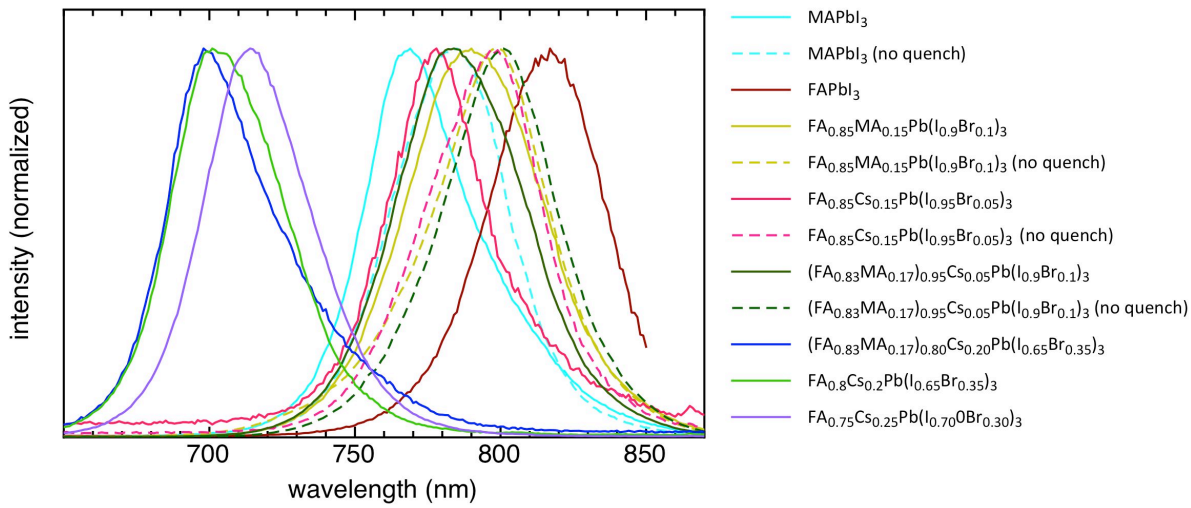

Figure S3: Photoluminescence data of the perovskite films in this work. The films were deposited on glass.

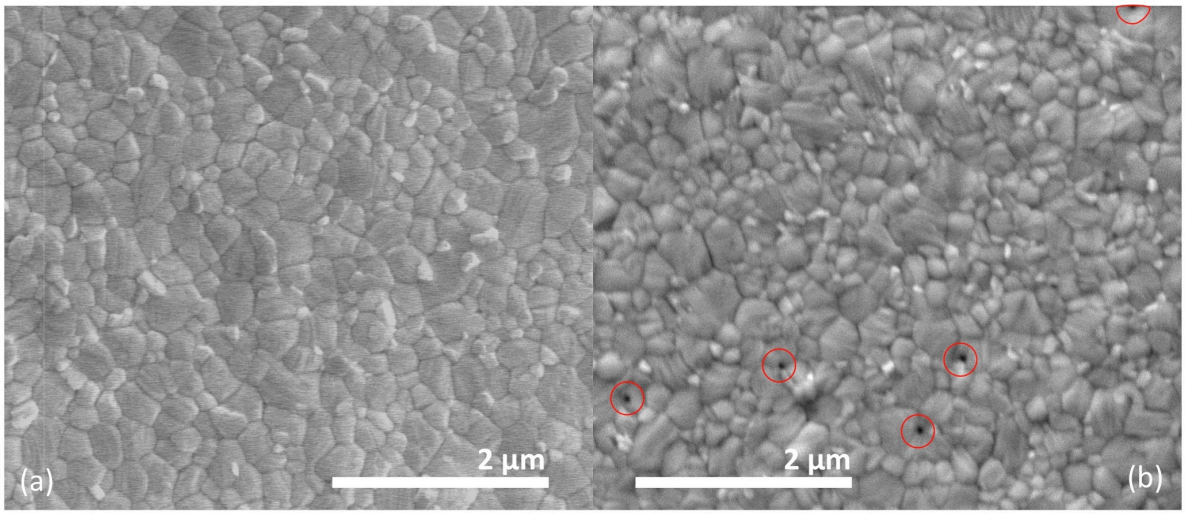

Figure S4: SEM images of $MAPbI_3$ films processed by CAGQ (a) from DMF:DMSO 9:1 and (b) from pure DMF. It is clear that the film made in absence of DMSO is less neat and contains pinholes (indicated by red circles), causing reduced FF and V_{oc}.

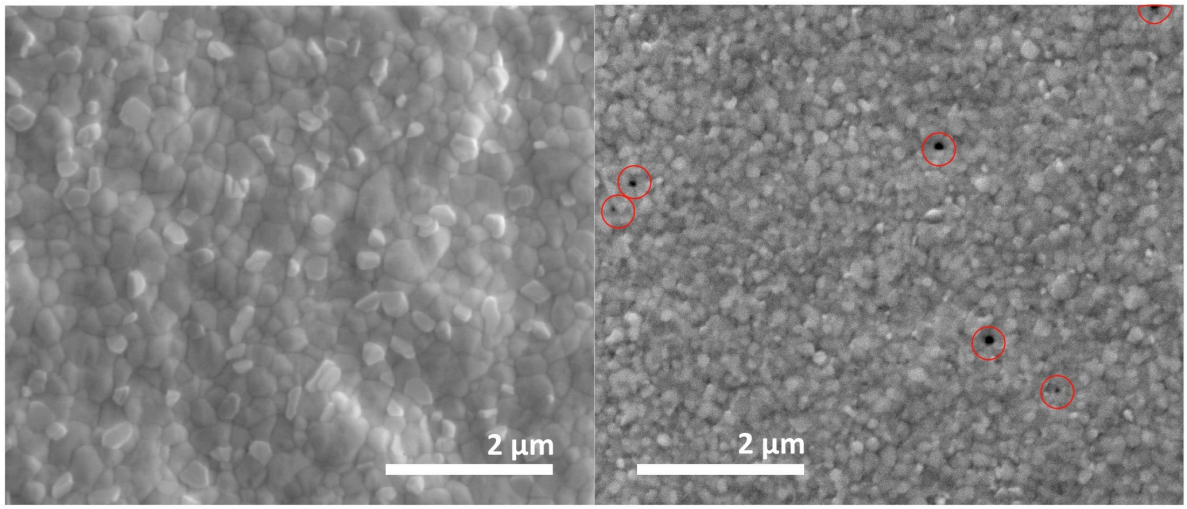

Figure S5: SEM images of $(FA_{0.83}MA_{0.17})_{0.95}Cs_{0.05}Pb(I_{0.9}Br_{0.1})_3$ films processed by CAGQ (a) from DMF:DMSO 9:1 and (b) from pure DMF. In the absence of DMSO, the crystallites are considerably smaller, and pinholes are clearly visible (indicated by red circles).

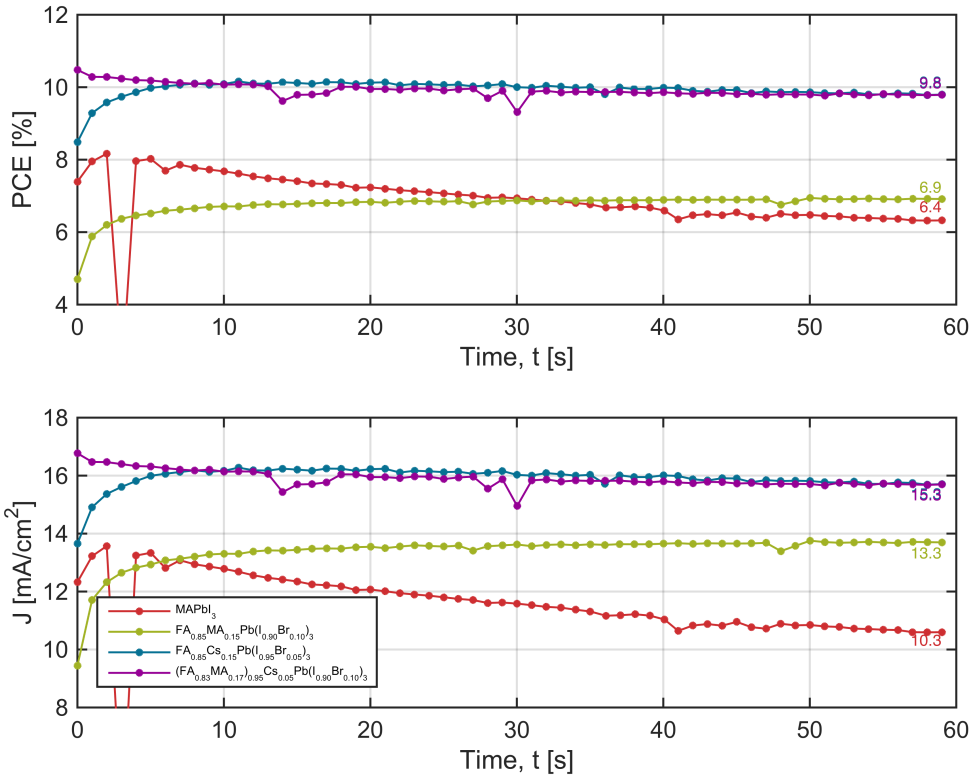

Figure S6: Stabilized power output curves and corresponding current density curves at maximum power point for the best non-CAGQ devices in n-i-p architecture (devices 1-4).

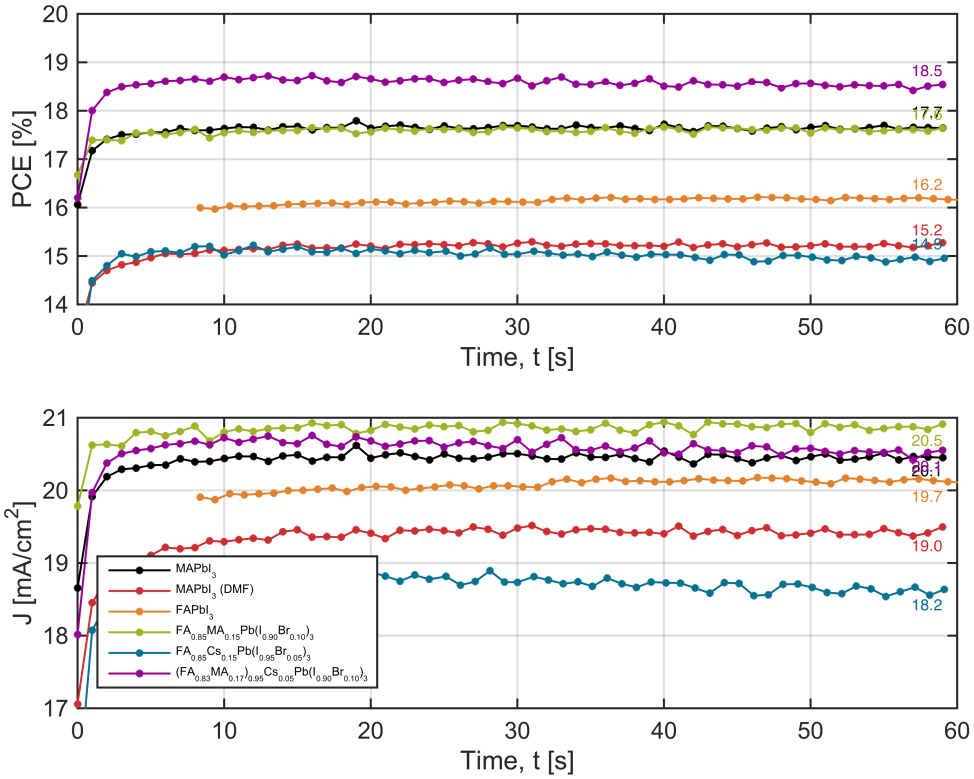

Figure S7: Stabilized power output curves and corresponding current density curves at maximum power point for the best CAGQ based devices in n-i-p architecture (devices 5-10).

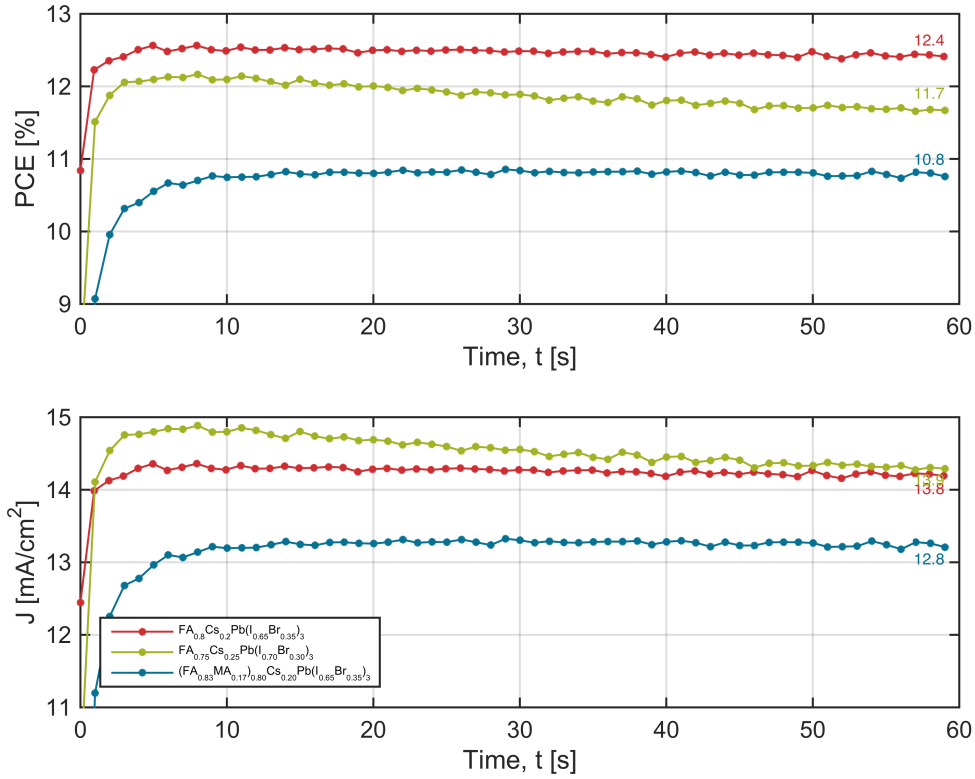

Figure S8: Stabilized power output curves and corresponding current density curves at maximum power point for the best CAGQ based large band gap devices in n-i-p architecture (devices 11-13).

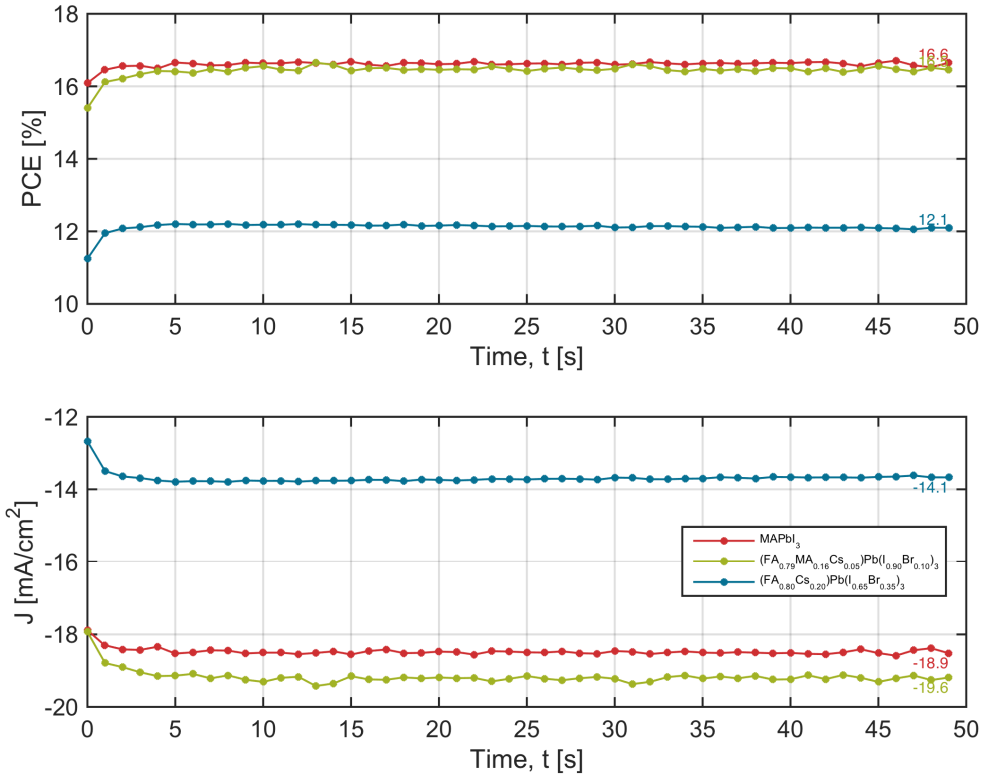

Figure S9: Stabilized power output curves and corresponding current density curves at maximum power point for the best CAGQ based devices in p-i-n architecture (devices 14-16).

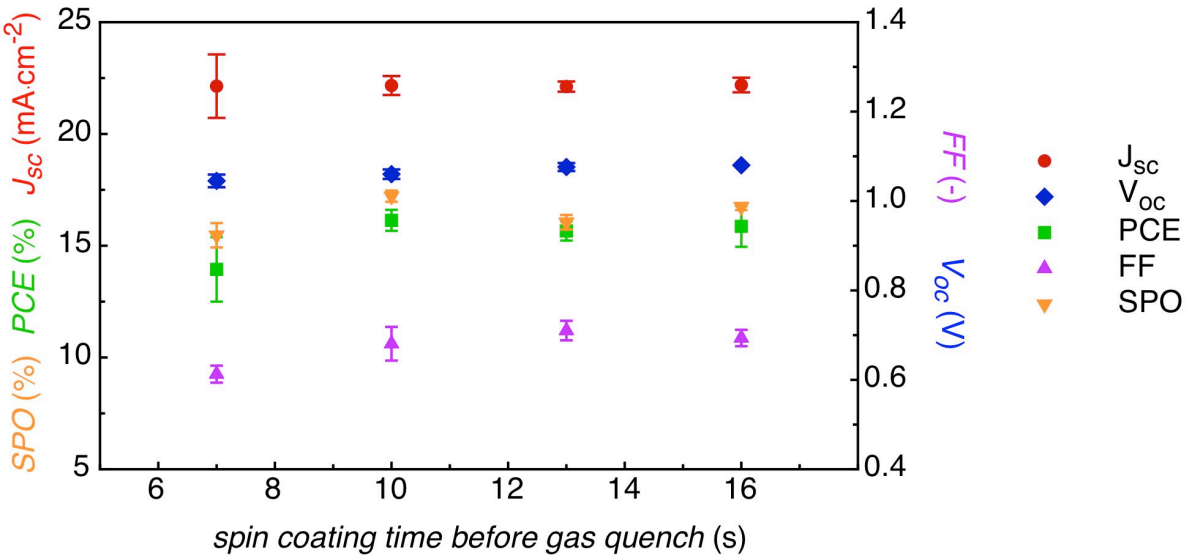

Fig. S10: Comparison of photovoltaic parameters of devices of the same batch with CAGQ deposited perovskite layers (here $FA_{0.85}MA_{0.15}Pb(I_{0.9}Br_{0.1})_3$), with different times between the start of the spin coating process and the start of the gas quench. The precursor concentration was 1.35M and the spin speed 3000 rpm.

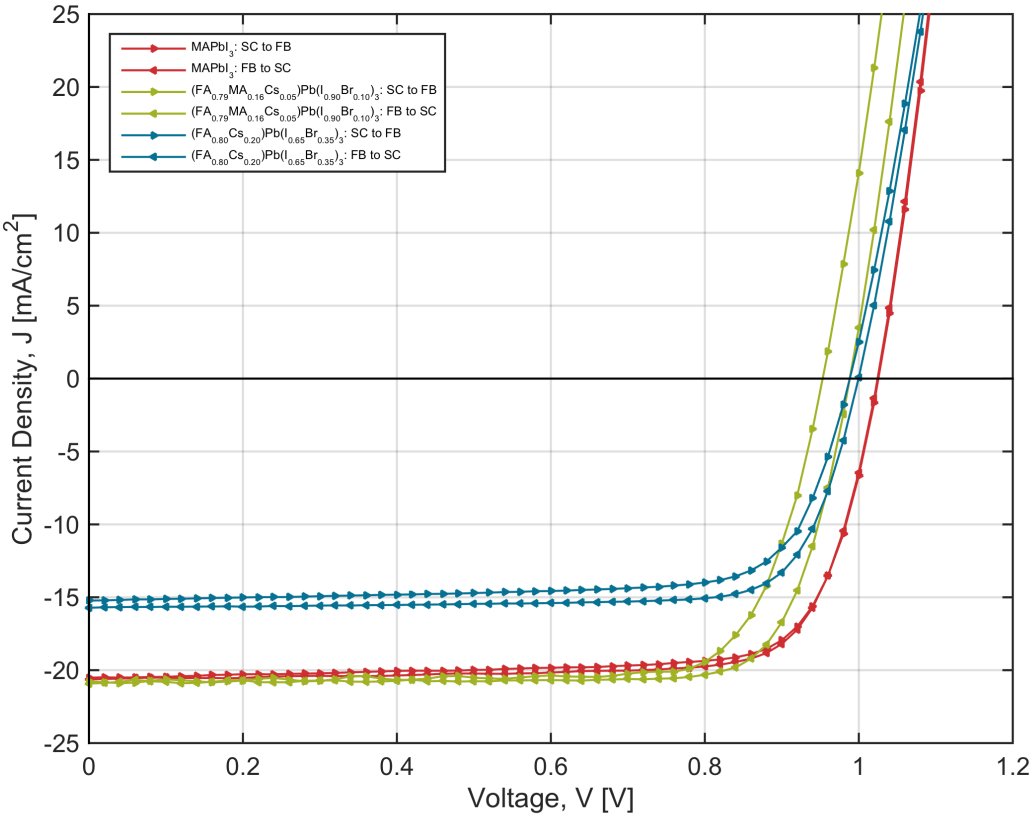

Fig. S11: Forward and reverse JV characteristics for the best p-i-n devices.

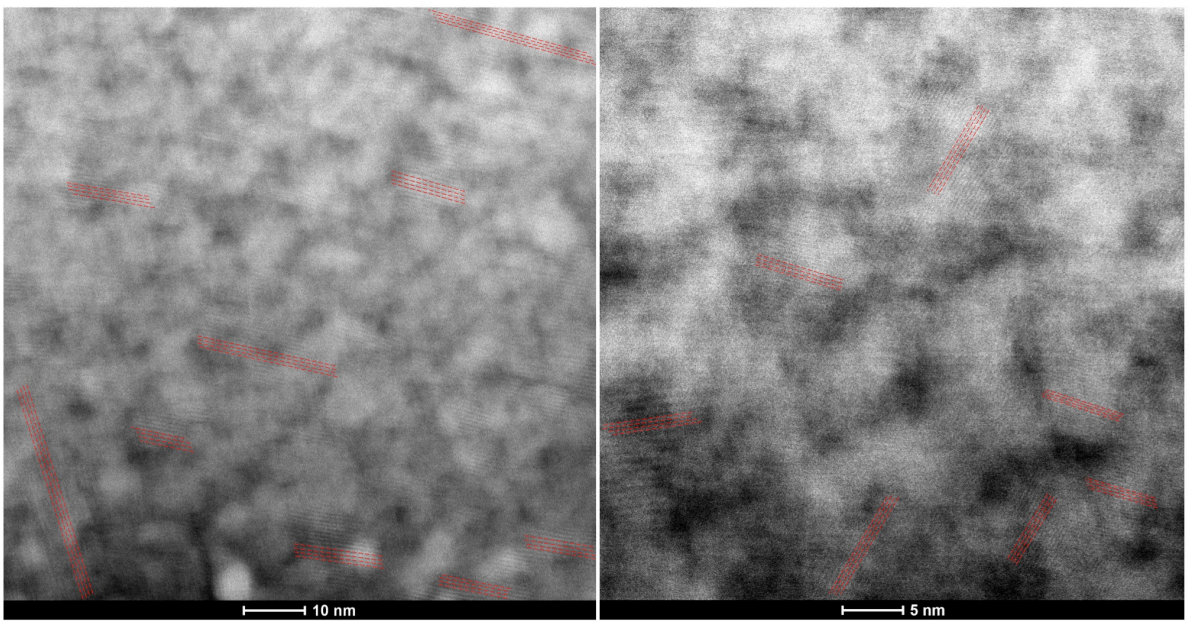

Fig. S12: High resolution STEM-HAADF images of CAGQ deposited $MAPbI_3$, where lattice fringes can be observed. Dashed red lines are added for a number of features as a guide to the eye. Some regions in the images appear featureless but this does not mean they are amorphous. If the orientation of crystalline domains is at an angle with the viewing direction, the density of atoms in projection is simply too large to resolve lattice planes as a result of the finite thickness of the FIB lamella.